Naval Research Laboratory
Washington, DC 20375-5320

NRL/7320/MR—2023/6

Development of Spatially Varying Parameters for Arctic Landfast Ice

RICHARD A ALLARD
ELIZABETH DOUGLASS
DAVID HEBERT
GLEB PANTELEEV

Ocean Dynamics and Prediction Branch
Ocean Sciences Division

September 21, 2023

REPORT DOCUMENTATION PAGE

Form Approved
OMB No. 0704-0188

1. REPORT DATE *(DD-MM-YYYY)*	**2. REPORT TYPE**	**3. DATES COVERED** *(From - To)*
21-09-2023	NRL Memorandum Report	

4. TITLE AND SUBTITLE

Development of Spatially Varying Parameters for Arctic Landfast Ice

5a. CONTRACT NUMBER

5b. GRANT NUMBER

5c. PROGRAM ELEMENT NUMBER

6. AUTHOR(S)

Richard Allard, Elizabeth Douglass, David Hebert, and Gleb Panteleev

5d. PROJECT NUMBER

5e. TASK NUMBER

5f. WORK UNIT NUMBER
6B20

7. PERFORMING ORGANIZATION NAME(S) AND ADDRESS(ES)

Naval Research Laboratory
4555 Overlook Avenue, SW
Washington, DC 20375-5320

8. PERFORMING ORGANIZATION REPORT NUMBER

NRL/7320/MR--2023/6

9. SPONSORING / MONITORING AGENCY NAME(S) AND ADDRESS(ES)

Office of Naval Research
One Liberty Center
875 N. Randolph Street, Suite 1425
Arlington, VA 22203-1995

10. SPONSOR / MONITOR'S ACRONYM(S)

ONR

11. SPONSOR / MONITOR'S REPORT NUMBER(S)

12. DISTRIBUTION / AVAILABILITY STATEMENT

DISTRIBUTION STATEMENT A: Approved for public release; distribution is unlimited.

13. SUPPLEMENTARY NOTES

14. ABSTRACT

This report describes the development of spatially varying landfast ice parameters and a variational algorithm for the optimization of these coefficients for the Arctic Ocean into the Community Sea Ice Model (CICE6). The CICE6 model code was modified in the generalized form and can be used for incorporation of spatial variability of other CICE6 model parameters. For the variational optimization of the landfast ice parameters we adopted an iterative Conjugate Gradient (CG) algorithm, which requires the knowledge of the cost function and it's gradient on each iterative step. In order to increase the computational efficiency we utilized the reduced space approach, where the limited number of the coefficients define the landfast ice in the large area. In addition, the entire Arctic Ocean was subdivided into 9 regions, where landfast ice was observed during the last two decades. The optimization of the landfast ice parameter was conducted separately for each region through the minimization of the difference between observed and CICE6 model generated landfast area. Comparisons are made between modeled landfast ice and observations for 9 Arctic regions.

15. SUBJECT TERMS

Landfast ice CICE6 Conjugate gradient
NIC Optimization Arctic

16. SECURITY CLASSIFICATION OF:			**17. LIMITATION OF ABSTRACT**	**18. NUMBER OF PAGES**	**19a. NAME OF RESPONSIBLE PERSON**
					Richard Allard
a. REPORT	**b. ABSTRACT**	**c. THIS PAGE**	U	26	**19b. TELEPHONE NUMBER** *(include area code)*
U	U	U			(228) 688-4894

This page intentionally left blank.

Table of Contents

List of Figures

This page intentionally left blank.

1. Introduction

In this report, we describe the novel development of the Community Ice CodE (CICE6) Sea Ice Model through the incorporation of spatially varying landfast ice (LFI) parameters in the Arctic Ocean. We adopted an iterative Conjugate Gradient (CG) algorithm for the variational optimization of LFI parameters. In order to increase computational efficiency we utilized the reduced space approach, where a limited number of coefficients define the LFI in the large area. In addition, the entire Arctic Ocean was subdivided into 10 regions where LFI was observed during the last two decades. The optimization of the LFI parameters was conducted separately for each region through the minimization of the difference between LFI observed by the U. S. National Ice Center (USNIC) and CICE6 model generated LFI area. We then tested these newly developed LFI coefficients by running CICE6 model and comparing against the observed Arctic LFI extent. The new CICE6 code with spatially varying LFI formulation is planned to be incorporated into the Navy's sea ice modeling systems.

2. Background

LFI, sometimes referred to as *fast ice*, is ice that can be fastened to the coast in shallow water depths and is stationary. This is in contrast to *pack ice*, which drifts due to wind and ocean forcing. LFI can form near the coast in the fall and usually stays nearly immobile for a period of months until breakup in late-spring or early-summer. Studies show that LFI can extend from the coast to water depths up to 100 meters and occupies a significant portion of the Siberian Shelf including the Kara, Laptev and East Siberian seas (Antonova 2011) as well as along the coast in the Chukchi and Beaufort Seas and in the multiple straits and channels of the Canadian Archipelagos (Mahoney et al., 2007, Ryan and Münchow, 2017). The LFI boundary determines the offshore position of polynyas and flaw leads, can affect the stability of the Arctic halocline, and can lead to a thinner coastal ice cover as only thermodynamic growth occurs (no dynamic effects).

Except in landlocked regions, the extent of LFI is largely limited by local bathymetry and the depth to which the keels of pressure ridges extend below the water. As a result, despite the large differences in overall distance from shore, the seaward edge of LFI in most regions of the Arctic is usually found in 15-30 m of water (Granskog et al., 2006; Mahoney et al., 2014; Selyuzhenok et al., 2015, Mahoney, 2018). In some cases, grounded icebergs may allow LFI to extend into waters deeper than 100 m along the coasts of Greenland, northern Canada, Severnaya Zemlya, and Svalbard (Jacobs et al., 1975; Divine et al., 2004).

In water depths exceeding 40-50m, LFI cannot form by grounding. In areas such as the Canadian Archipelago where LFI is present for an extended period, it forms due to tensile strength (see Sec. 3). In the Arctic, LFI forms on the shallow shelf regions, where grounded ice keels can serve as anchor points, or between islands and in the narrow straits, where restrictive geometry allows the formation of the ice bridges or "arches".

There are several estimates of the maximum depth of sea ice keels. Duncan et al., 2018, analyzed the sea ice ridges and found that the maximum sail height ranged from 2.1 to 4.8m, suggesting a maximum sea ice keel of ~45m. Several authors analyzed LFI formation along the Alaskan coast and reported that the grounded LFI was usually observed in 15-30m of water (Granskog et al., 2006; Mahoney et al., 2014; Selyuzhenok et al., 2015). Mahoney (2018) speculates that "grounded icebergs may allow LFI to extend into waters deeper than 100 m along the coasts of Greenland, northern Canada, Severnaya Zemlya, and Svalbard (Jacobs et al., 1975; Divine et al., 2004)." Our analysis of ice keels in the Beaufort Sea (Fig. 1) shows that ice keels do not attain a depth of 30 m based on Upward Looking Sonar (ULS) data for the period of 2007-2021.

Manuscript approved September 19, 2023.

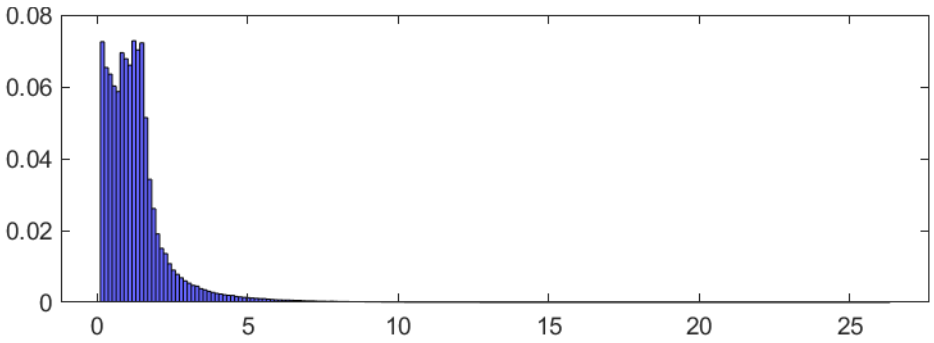

Fig. 1 *PDF Analysis of the 3 WHOI ULS sea ice draft from moorings in the Beaufort Sea for the period of 2007 – 2021 shows that ice keels do not exceed 30m*

The process of the LFI formation controls the circulation and physical processes of the sea water in the shelf and continental slopes (Itkin et al., 2015) and significantly affects any maritime activity and shipping in the Arctic. The Navy's ice models presently do not account for LFI. This results in non-realistic ice drift and circulation patterns and improper polynya and lead formation.. Fig. 2a shows MODIS imagery for April 19, 2017 with the U.S. Navy's Global Ocean Forecast System (GOFS 3.1) ice drift overlaid (image from the (USNIC)). The red line denotes the demarcation between pack ice and LFI to the south. Note that there should not be any ice motion with the LFI. Figure 2b depicts GOFS 3.1 ice concentration. Note the difference in the actual lead openings/polynyas indicated by the green oval on the left versus the modeled openings (yellow oval) on the right. Without the inclusion of LFI in Navy models, polynya placement is incorrect.

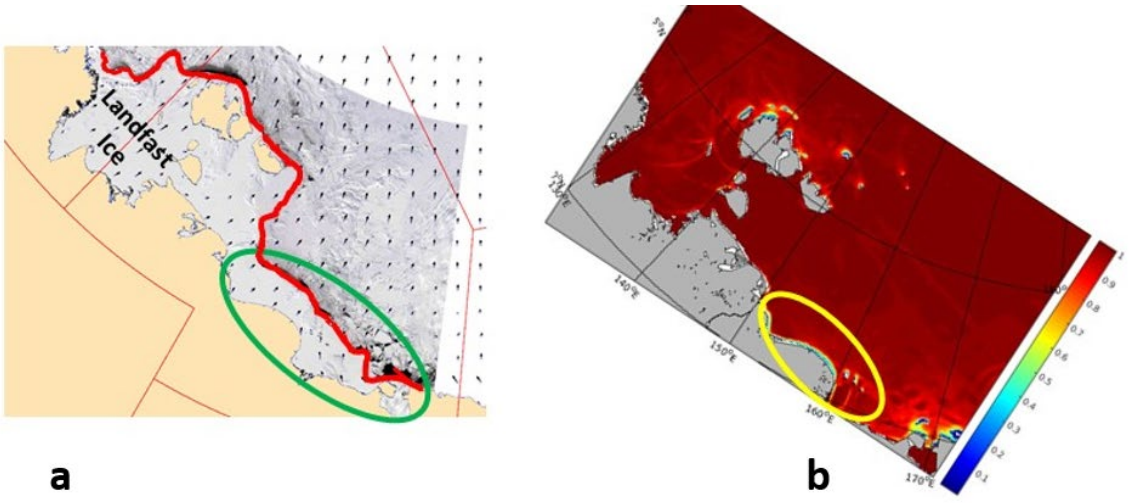

Fig. 2 *a) USNIC MODIS imagery depicting LFI extent (red line) for East Siberian Sea. GOFS 3.1 ice drift vectors overlaid. Green oval highlights boundary between LFI and pack ice. Dark black colors denote low concentration region or polynyas. b) GOFS 3.1 ice concentration (%). Yellow oval shows similar area as green oval but note that no low ice concentration or polynyas are present in this model which does not contain LFI.*

3. CICE6 Version Used in this Study

In this study, we use the CICE 6.1.4 model (hence referred to as CICE6) developed by the CICE Consortium[1]. CICE6 is the model used in the Navy's Earth System Prediction Capability (ESPC) V2 and contains the LFI parameterization developed by Lemieux et al. (2015, 2016). In the studies performed and discussed in this report, CICE6 is run in an uncoupled "standalone" mode where input files for atmospheric and oceanic boundary conditions, as well as sea ice boundary conditions, are provided by external files.

The dynamical core of the CICE6 model used in this study is the Elastic-Viscous-Plastic (EVP) ice physics. EVP is a numerically efficient method of discretizing the sea ice momentum equation by allowing elastic waves that are damped over several iterations. (Full details of the EVP method are provided in Hunke et al., 2008). The stress $\boldsymbol{\tau}$ exerted on ice through its interaction with bottom $\boldsymbol{\tau}_\mathbf{b}$, atmosphere $\boldsymbol{\tau}_\mathbf{a}$ and the ocean $\boldsymbol{\tau}_\mathbf{w}$ are:

$$\rho h A\left(\partial_t + \tilde{f}k\times\right)u = \mathrm{div}(\boldsymbol{\sigma}) + \boldsymbol{\tau}_b + \boldsymbol{\tau}_a + \boldsymbol{\tau}_w \tag{1}$$

$$\tilde{T}_d\,\partial_t\boldsymbol{\sigma} + e^2\boldsymbol{\sigma} + 0.5\mathrm{tr}\boldsymbol{\sigma}(1-e^2)\mathbf{I} = P_\mathrm{p}[(1+k_\mathrm{T})\dot{\boldsymbol{\epsilon}} - 0.5\Delta(1-k_\mathrm{T})\mathbf{I}]/\Delta^* \tag{2}$$

$$\partial_t h = \mathrm{div}(h\boldsymbol{u}) \tag{3}$$

$$\partial_t A = \mathrm{div}(A\boldsymbol{u}) \tag{4}$$

Here, div and tr are the divergence and trace operators; $\boldsymbol{k}$ is the vertical unit vector; $\mathbf{I}$ is 2x2 identity matrix; h, A and $\boldsymbol{u}=\{u,v\}$ are 2D fields of ice thickness, concentration and velocity; $\tilde{T}_d, P_P$, k_T and e are empirical parameters that define the EVP elastic damping scale of sea ice, its internal pressure, isotropic tensile strength and the yield curve axes ratio, respectively.

$\boldsymbol{\sigma}$ and $\dot{\boldsymbol{\epsilon}}$ are the 2D ice stress and deformation rate tensors:

$$\boldsymbol{\sigma} = \begin{bmatrix}\sigma_{xx} & \sigma_{yx}\\ \sigma_{xy} & \sigma_{yy}\end{bmatrix};\ \dot{\boldsymbol{\epsilon}} = 0.5\begin{bmatrix}2\partial_x u & \partial_x v + \partial_y u\\ \partial_x v + \partial_y u & 2\partial_y v\end{bmatrix} \tag{5}$$

The scalar field used for normalizing the right-hand side in (2) is computed using the following expression (e.g., Hunke, 2001):

$$\Delta(\dot{\boldsymbol{\epsilon}}) = \frac{1}{e}[(e^2-1)(\mathrm{tr}\dot{\boldsymbol{\epsilon}})^2 + 2\mathrm{tr}(\dot{\boldsymbol{\epsilon}}^2)]^{0.5} \tag{6}$$

To avoid numerical singularities at $\dot{\boldsymbol{\epsilon}} = 0$, the values of Δ are limited from below by the additional parameter $\tilde{\Delta}^* = 10^{-10}s^{-1}$, so that $\tilde{\Delta}^*(\dot{\boldsymbol{\epsilon}}) = \max(\Delta, \tilde{\Delta}^*)$.

CICE6 includes two ice strength formulations: one proposed by Hibler (1979) and one proposed by Rothrock (1975). We used the formulation proposed by Hibler (1979), where the internal ice pressure, P_P is related to ice thickness and concentration:

$$P_p = P^* h A e^{-\alpha(1-A)} \tag{7}$$

The bottom and ocean stresses, $\boldsymbol{\tau}_\mathbf{b}$ and $\boldsymbol{\tau}_\mathbf{w}$, in Eq. (1) are parameterized in accordance with Lemieux et al. (2015, 2016) and Hunke and Lipscomb (2008):

$$\boldsymbol{\tau}_b = \begin{cases} 0, & h \le h_c \\ k_2\left(\frac{u}{|u|+u_o}\right)e^{-C_b(1-A)}, & h > h_c \end{cases} \tag{8}$$

[1] https://github.com/CICE-Consortium/CICE

$$\boldsymbol{\tau}_w = -C_w \rho_w A |u - u_w| R_\Theta (\boldsymbol{u} - \boldsymbol{u}_w) \quad (9)$$

Where $h_c = A h_w / k_1$ is critical depth, h_b is the ocean depth, R_Θ is the 2×2 matrix rotating the velocity vector by the turning angle Θ counterclockwise, $u_o = 10^{-5}$ m/s and $\boldsymbol{u_w}$ is the water velocity.

The basal stress term $\boldsymbol{\tau_b}$ in the momentum equation (1) was proposed by Lemieux et al. (2015, 2016). If the mean ice thickness h is less than the critical ice thickness h_c, then grounding does not occur, basal stress is set to 0, and LFI does not form. k_2 is the maximum basal stress parameter set to 15. C_b is a constant set to 20, and ice concentration assumed to be almost 100%. In our tests we used h_c = 30m, which is the CICE6 default value.

Thus, the parameter k_1 defines the area where the grounding effect may take place, while parameter k_2 plays the role of the sea ice-bottom friction. In the CICE6 formulation of Lemieux et al., (2015, 2016), k_1 and k_2 are constants and equal to 8 and 15 N/m^{-3} respectively.

The uniaxial and tensile strength (T) based on König Beatty & Holland (2010) was added to CICE6 to represent the LFI arching mechanism observed in the deep regions in the Kara Sea and Canadian Archipelagoes (Lemieux et al, 2016). In this parameterization $T = k_T P_p$, where k_T is a parameter that characterizes the amount of tensile strength T, and P_p represents the compressive ice strength. Tensile strength will be described in greater detail in Sec. 8. The default values of the parameters k_1, k_2, k_T were defined by Lemieux et al. (2015, 2016) in multiple numerical experiments with relatively coarse resolution model (~12.5 km in central Arctic) and LFI observation for the Kara, Laptev, East Siberian and Beaufort seas.

4. Landfast Ice Observations

Digital sea ice charts for the entire Arctic Ocean are produced by the National Oceanic and Atmospheric Administration (NOAA)[2]. There are also regional sea ice charts produced by the Canadian Ice Center[3] and the National Weather Service Alaska Sea Ice Program[4]. All chart files are written in shapefile format which can be read by ArcGIS (or other) software and utilize the SIGRID-3 vector archive format for the designation of the different sea ice categories (e.g. pancake, cake, sea ice floes, landfast ice) and sea ice concentration (SIGRID-3, 2010). We analyzed the observations from each database, but ultimately chose the data from NOAA as the most comprehensive and easily accessible source of LFI information. Figure 3a presents an example of an analysis by the National Ice Center[5] for the East Siberian Sea on January 13, 2023. Figure 3b shows a LFI analysis off the northern Alaskan coast on January 26, 2023. In both figures grey shading indicates LFI.

All LFI polygons from NOAA charts were extracted for the period of 2003-2021 and interpolated onto the Global Ocean Forecast System (GOFS 3.5) 1/25° grid (~1.75 km at the North Pole). (See Table 1 for list of all regions used in this study). The derived LFI maps were used for statistical analysis with the goal to identify the regions where the LFI could be potentially formed.

[2]Data available at ftp://sidads.colorado.edu/pub/DATASETS/NOAA/G10033/north/weekly/shapefiles
[3]Data available at https://www.canada.ca/en/environment-climate-change/services/ice-forecasts-observations/latest-conditions.html
[4]Data available at https://www.weather.gov/afc/ice
[5]Data available at https://usicecenter.gov/Products

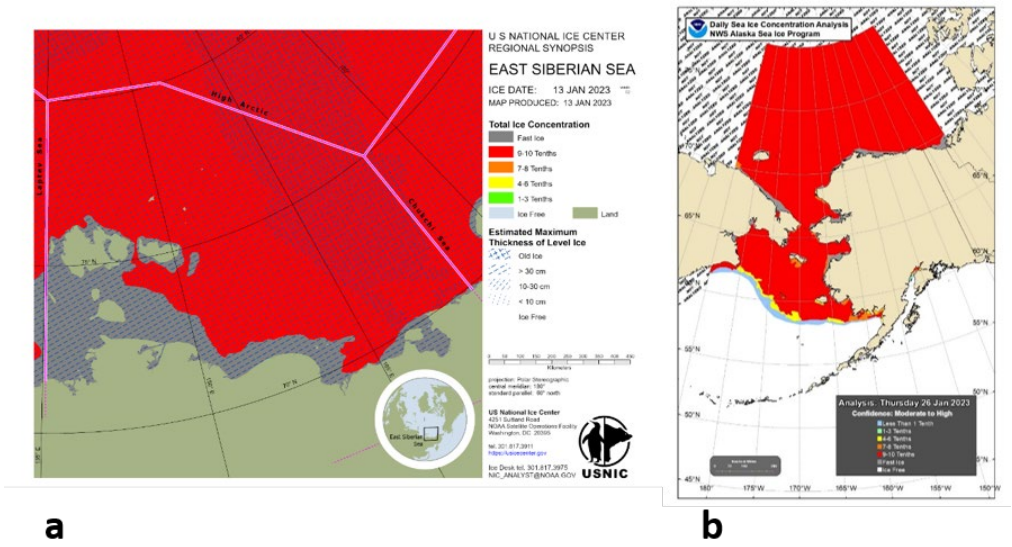

Fig. 3 *a) USNIC ice chart for the East Siberian Sea January 13, 2023. Ice concentration (tenths of a percent) is shown in red; grey shade denotes LFI. b) NWS Alaska Sea Ice Program ice analysis for January 26, 2023. Grey shading along northern Alaskan coast denotes LFI.*

We analyzed the LFI chart data for the period of 2007 – 2020 to determine the probability of LFI presence due to grounding in shallow water depths, less than 35m (Fig. 4). Fig. 5a shows the probability of LFI due to grounding, which is controlled by coefficients k_1 and k_2. In this area the majority of LFI is close to land. However, the area of the LFI observations usually extend into deeper regions, where grounding is not realistic. It is reasonable to suggest that LFI formation in the deep regions is due to sea ice arching phenomenon. Fig. 5b depicts the probability of the formation of LFI in deep regions due to ice arching.

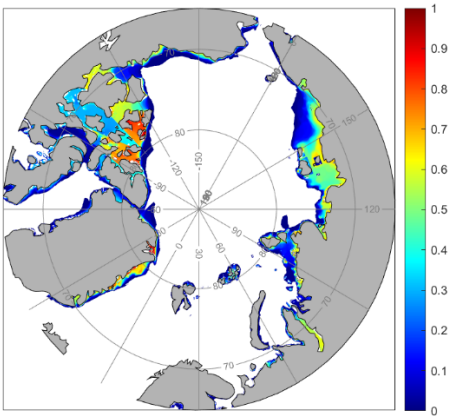

Fig. 4 Mean probability of the formation of the LFI in different regions of the Arctic Ocean. Taking into account that grounding LFI can be formed only in relatively shallow (<35m) regions, the LFI areas can be formally subdivided by the physical mechanism of the LFI formation discussed in Section 3.

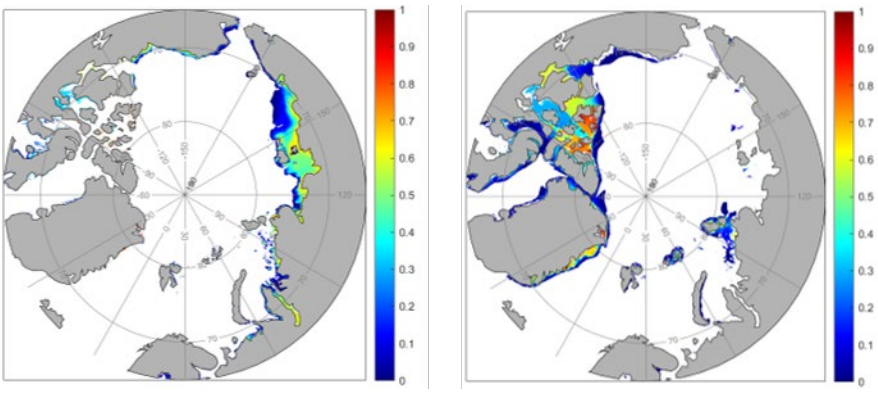

Fig. 5 a) The probability of the formation grounding LFI in the Arctic Ocean defined by grounding phenomenon, which is controlled by the coefficients $k_1(x)$ and $k_2(x)$; b) The probability of arching LFI formation in the deep regions of the Arctic Ocean controlled by coefficients $k_T(x)$.

5. Preliminary CICE6 Testing

We performed preliminary testing of CICE6 with LFI using the default parameter settings without spatially varying parameters. In order to locate LFI in an ice field we use two criteria: 1) ice must be present, and 2) ice cannot be moving. In practice, this is defined as ice concentration above 15%, and ice speed less than 0.0005 m/s for at least 14 consecutive days (as proposed by Lemieux et al. (2015). If these conditions are met, a location is considered to have LFI. Using these criteria, we can define the number of days during which a location has LFI present during a given time series.

LFI was examined using two model systems. The first model system considered was the most recent version of the Global Ocean Forecasting System (GOFS) 3.5. This system consists of the HYCOM ocean model coupled with the CICE 5.1.2 ice model, and has horizontal resolution of 1/25° (~1.75 km at the North Pole). The second model system considered is from an uncoupled, standalone run of CICE6. This simulation had the same horizontal resolution as GOFS 3.5 (1/25°), and used GOFS 3.5 ocean files as an ocean forcing data (SST, SSS, ocean surface currents). The CICE6 model used the default parameterization values for LFI, $k_1 = 8$, $k_2 = 15$, and $k_T = 0.2$.

In all cases the dates considered were September 2017 through May 2018. These dates were chosen because September (with minimum ice) marks the beginning of the freezing season and May is generally when ice begins to break up in the spring. Thus, one would not expect formation of new LFI after May.

Figure 6a depicts the LFI extent from CICE6 versus GOFS 3.5 and the USNIC analyzed LFI extent. Since GOFS 3.5 system uses CICE 5.1.2, it does not include a parameterization for LFI, and as a result there is almost no LFI seen. We see a reasonable comparison between CICE6 and the USNIC analysis. Overall, CICE6 shows an under-prediction especially beginning in May 2018. Fig. 6b depicts a time series of the LFI for the same period but for the Canadian Archipelago.

In another qualitative test to examine the robustness of CICE6 using default LFI parameters, we compared the LFI extent on April 17, 2018 versus imagery provided by the USNIC. In Fig. 7, we compare GOFS 3.5 analysis (no LFI included) versus a CICE6 analysis. CICE6 shows a reasonable agreement in the LFI extent (green line) versus the LFI delineation visible in the MODIS image. In addition, polynyas or flaw leads are visible in CICE6 (which agree well with MODIS image), but are not present in GOFS3.5 analysis. In aggregate, these tests provided a valuable demonstration that we could move forward in the development of spatially-varying LFI parameters using CICE6.

6. Experimental Setup

We defined 10 regions in the Arctic to perform LFI optimization experiments: Laptev Sea, East Siberian Sea (4 sub-regions), Chukchi Sea (3 sub-regions), Beaufort Sea and the Canadian Archipelago (red boxes in Figure 8). The number and spatial extent of the domains is constrained by two factors. First, due to limited computational resources, each region should be as small as possible and not include a large portion of the deep areas where LFI is not observed. Second, we suggest that spatial variability of the rheological parameters k_1 and k_2 is controlled by geological (sediments) factors and coastline configuration and have a typical scale of about 100 km (e.g. Nikishin et al., 2019). These limitations suggest that spatial variability of the parameter k_1 for each region may be defined by 5-8 unknown parameters k_1^i, i=1:5(8), which should be optimized. The relatively small number of the unknown k_1^i parameters allows us to reach a reasonable computational efficiency on the available HPC systems.

Figure 8 depicts the historical poleward LFI extent by a thick black dashed line. The 10 regional domains were setup to ensure LFI seasonal variability was captured. These 10 regional domains are an exact subset of the GOFS 3.5 1/25° grid. The optimization experiments were designed to generate spatially varying grounding (k_1) and tensile strength (k_T) coefficients for incorporation into Arctic arrays in CICE6 for use in the global GOFS 3.5 and ESPC V2 deterministic modeling systems (both 1/25°). Table 1 depicts the 10 sub-regions used in this study along with the dimensions of the 1/25° grid. Due to its large size, we divided CA1 into 4 smaller regions (e.g., CA1-1, CA1-2 etc).

For each set of optimization experiments, a standalone CICE6 grid was generated which included bathymetry files for each region. A set of scripts was developed to extract ocean forcing, ice restart and atmospheric forcing for the periods of October 1, 2015 – August 1, 2016 and October 1, 2017 – August 1, 2018. HYCOM and CICE output were used to generate initial/boundary forcing for all regional CICE6 runs. Additional years of optimization experiments were planned, but due to limited computational resources, we performed the experiments for two separate 10-month periods. For the period of 2015-2016 we used the GOFS 3.1 (1/12°) reanalysis model output; GOFS 3.5 (1/25°), model output (which includes tides) was used for the period of 2017-2018. The NAVy Global Environmental Model (NAVGEM) was used as atmospheric forcing for both sets of experiments.

Table 1. *The 10 sub-regions used in our optimization experiments. CA1 is divided into 4 smaller regions to facilitate faster turnaround on Navy HPC computers. Grid resolution is 2km for all regions.*

REGION	NX	NY
	rows	columns
BE7	336	608
CS1	280	360
CS2	160	270
CS3	330	408
ESS1	352	384
ESS2	270	440
ESS3	280	384
ESS4	312	512
LS1	664	384
CA1-1	192	320
CA1-2	150	160
CA1-3	192	328
CA1-4	192	224

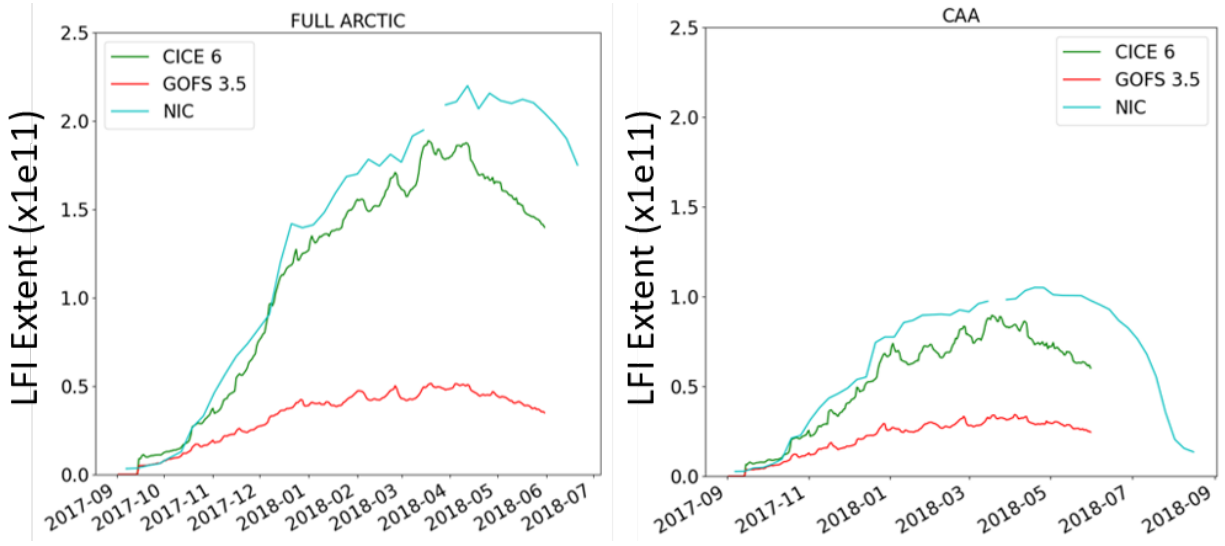

Fig. 6 *a) Arctic-wide LFI extent (m^2) for the period of September 2017 – June 1, 2018. Red line denotes GOFS 3.5 results without LFI. Green line represent CICE6 results with LFI turned on but using defaults without spatial variation. Cyan line depicts USNIC analyzed LFI extent. B) Same but for Canadian Archipelago.*

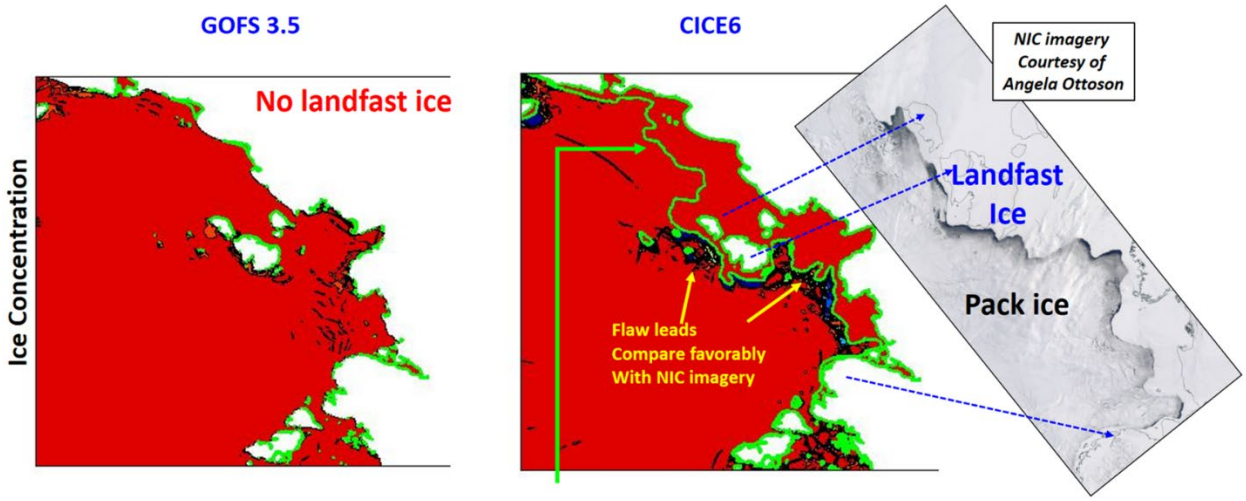

Fig. 7 *Left) GOFS3.5 ice concentration (100% shown in red) on April 17, 2018. LFI was not turned on for this simulation. Middle) CICE6 with LFI turned on. Green line depicts USNIC LFI extent. Dark regions indicate low ice concentration where polynyas have formed poleward of LFI edge. Right: MODIS imagery for the same date showing very good agreement with modeled LFI.*

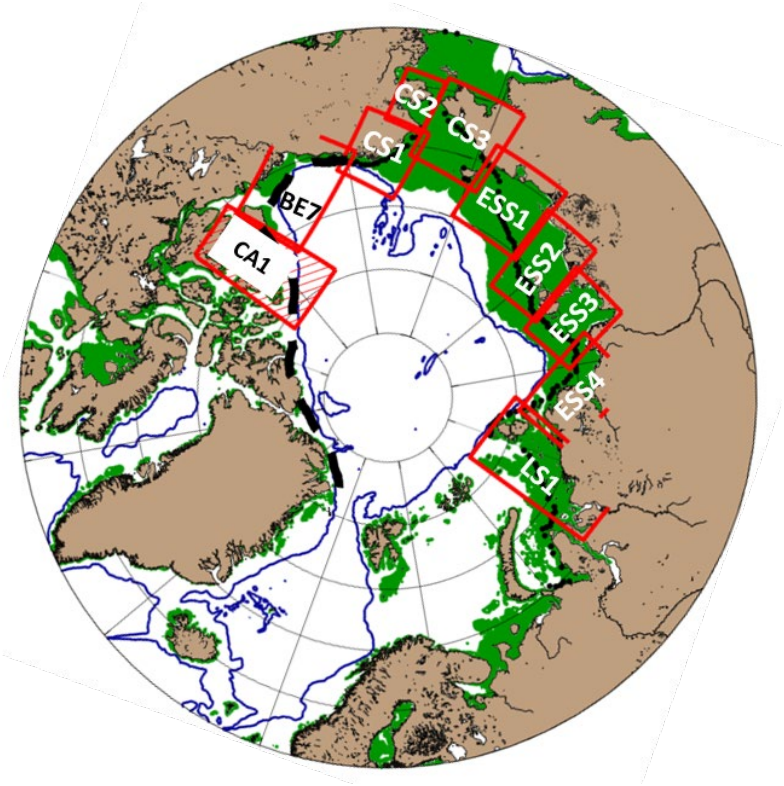

Fig. 8 *Arctic domain showing the 10 sub-regions used in this study. ESS denotes East Siberian Sea, CS represents Chukchi Sea, LS1 represents Laptev Sea, and CA represents the Canadian Archipelago. Green shading represents water depths less than 100m. The blue line represents the 1000m isobath. Black dashed line represents the maximum poleward LFI extent based on historical data. Dashed red shading for CA1 indicates a region where tensile strength (k_t) optimization was performed.*

7. Optimization Algorithm

Optimization of the sea ice model parameters can be conducted via various approaches. The optimal way would be to use a complete adjoint of the sea ice model and define model parameters through the conventional 4DVAR data assimilation (e.g. Panteleev et al, 2020). However due to the absence of the tangent linear and adjoint model for CICE6 model, we had to apply a different approach.

Formally, the simplest option could be a Bayesian stochastic inversion, based on one of the versions of the Simulated Annealing (SA) algorithms (Pincus, 1970, Khachaturyan et al, 1979). The advantage of the Bayesian stochastic approach is the possibility to find an absolute minimum in the presence of the multiple local minimums. However, even the most advanced versions of the Bayesian stochastic approaches (e.g. Very Fast Simulation Annealing (VFSA)) suffer from slow convergence, difficulties in tuning of its parameters, and a time-consuming procedure of the generation of the multivariate stochastic variables in the multidimensional case (e.g. Ilich, 2014). An alternative approach which we opted is to use the Conjugate Gradient (CG) algorithm for optimization of the spatially varying LFI parameters. This requires the definition of the initial first guess values, algorithms for calculation of the cost function of n variables, $f(x)$, and its gradient $-g_k$. The CG algorithm allows for the minimization of the quadratic cost function

$$\min(f(x)) \tag{10}$$

through the sequential iterative process

$$d_k = \begin{cases} -g_k & , k = 1 \\ -g_k + \beta_k d_{k-1} & , k \geq 2 \end{cases} \tag{11}$$

$$x_{k+1} = x_k + \alpha_k d_k \quad (12)$$

where β_k is a scalar and α_k is a step length obtained by mean of a one dimensional search. β_k is defined using the Fletcher-Reeves formula:

$$\beta_k = \|g_k\|^2 / \|g_{k-1}\|^2 \quad (13)$$

The CG method can theoretically be viewed as a direct method. In the absence of round-off errors and minimization of the quadratic and monotonic cost function it produces the exact solution after a finite number of iterations, which is not larger than the dimension *n* of the minimization problem. In practice however, the CG algorithm usually requires more but still finite number of iterations (e.g. Gilbert and Nocedal, 1992*)*. The cost function $f(x)$ is defined as:

$$f(x) = \sum_{i_p} S_{i_p}^2 + \sum_{i_n} S_{i_n}^2 \quad (14)$$

where i_p *(or* i_n) are the indexes of the model cells, where the solution of the model generates (does not generate) ice, while landfast observations indicate the absence (presence) of LFI respectively. Similar to Lemieux et al. (2015), ice at a certain grid cell is considered landfast if its 2-week mean speed is smaller than 5×10^{-4} m s^{-1}.

In multiple numerical experiments we also evaluated other forms of the cost function (e.g. $f(x) = \sum_{i_p} S_{i_p}^2 + \sum_{i_n} S_{i_n}^2$) but found that the quadratic cost function (Eq. 14) provides the faster convergence. That is most-likely due to better convex properties of the quadratic cost function (Eq. 14).

The control vector of the spatially varying parameters was defined in reduced space for each regional sea ice model configuration (see Fig. 8) in the following empirical way. First, we defined regions $S^{k_{1/2/T}}$ where LFI could be formed with the probability large (0.1) according to the analysis of all historical sea ice chart data. (see Section 4). Second, the reduced vectors $\boldsymbol{k_{1/2/T}} = \{k_{1/2/T}^i, i = 1, N^R\}$ with first guess components $k_{1/2/T}^i$ were specified for the several locations uniformly distributed inside the regional CICE6 model domain (Figure 9a,b). Third, the spatially varying distributions of parameters $k_1(\boldsymbol{x}), k_2(\boldsymbol{x})$ and/or $k_T(\boldsymbol{x})$ were defined through the smooth interpolation into the regional model grid for the regions $S^{k_{1/2/T}}$, where LFI potentially can be formed.

$$k_{1/2/T}(\boldsymbol{x}) = \sum_{i=1}^{N^R} w_i \, k_{1/2/T}^i / \sum_{i=1}^{N^R} w_i \quad , \quad w_i = \exp(-\|x - x_i\|^2 / r^2) \quad (15)$$

The dimension N^R of the reduced space vectors $\boldsymbol{k_{1/2/T}}$ ranged between 3 and 8 elements. The correlation radius r was defined empirically in order to preserve smooth variability of the rheological parameters along the coast and ranged between 25 and 40 km. Finally, the derived spatial distribution was additionally smoothed with a Gaussian filter and correlation radius of 5 km in order to avoid sharp changes of the coefficients $k_1(\boldsymbol{x}), k_2(\boldsymbol{x})$ and/or $k_T(\boldsymbol{x})$ between LFI regions $S^{k_{1/2/T}}$ and other areas of the model domain where all coefficients $k_1(\boldsymbol{x}), k_2(\boldsymbol{x})$ and/or $k_T(\boldsymbol{x})$ were set to zero. Figure 9 illustrates the interpolation procedure from the reduced space of the vectors $\boldsymbol{k_{1/2/T}}$ to the model grid.

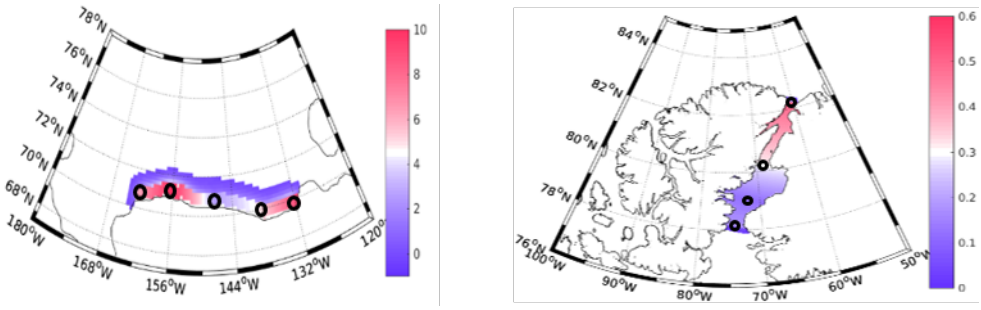

Fig. 9 Examples of the definition of the spatially varying coefficients (a) $k_1(x)$, $k_2(x)$, and (b) $k_T(x)$ in the corresponding reduced space defined by black dots and circles.

On each iteration, the gradients $g_k, k = 1, N^R$ can be approximately defined by perturbing the component of the control vector, running the CICE6 model for a period of 8-9 months (October 1-July or August 1), i.e. for the period of the intense formation of the LFI in the Arctic Ocean, and estimating the difference of the cost functions in the disturbed and non-disturbed solutions of the CICE6. Thus, for the estimation of the N^R gradients, we need to run the CICE6 model $N^R + 1$ times and simultaneous optimization of the all LFI parameters $[\boldsymbol{k_1}\ \boldsymbol{k_2}\ \boldsymbol{k_T}]$ requires $3N^R + 1$ model runs. For multiple regions (Figure 8) that could be computationally expensive and because of that we decided to separate the optimization of the grounding parameters $[\boldsymbol{k_1}\ \boldsymbol{k_2}]$ and tensile strength parameter $[\ \boldsymbol{k_T}]$.

In several numerical experiments we also analyzed the behavior of the cost function (14) with respect to the varying $\boldsymbol{k_2}$ parameter and fixed $[\boldsymbol{k_1}]$. It was found that the cost function (14) usually has a flat plateau when $\boldsymbol{k_2}$ increases past 15 N/m^3 (Figure 10).

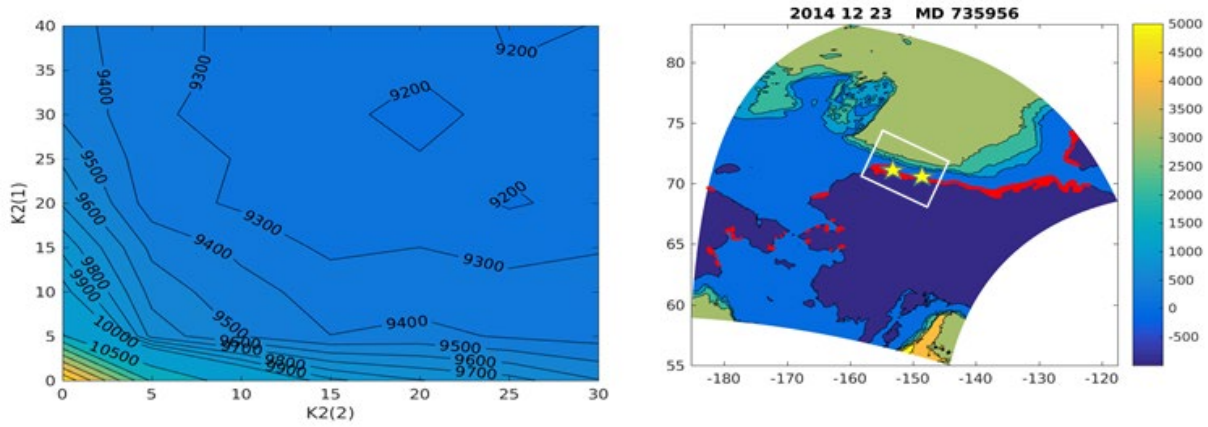

Fig. 10 a) The shape of the cost function (Eq. 14) in multiple numerical experiments conducted for the small regional model configured along the Alaska coast and controlled by two k_2^i parameters. b) model domain and location of the reduced space vector $k_2^i, i = 1,2$.

The physical explanation of the observed behavior of the cost function (Eq. 14) is straightforward. According to Lemieux et al. (2015), parameter k_2 plays the role of the bottom friction coefficient. Wind is the most important forcing in the stability of the LFI and it is reasonable to suggest that during the period of 2 weeks wind amplitudes near the coast have a similar maximum in different parts of the Arctic Ocean. Thus, k_2~15 N/m^3 provides sufficient friction to keep sea ice in place even for the strongest wind. Interestingly, a similar value was obtained in the numerical experiments with a different sea ice model (Lemieux et al, 2016). Because of that we chose to use the constant k_2=15 N m^3.

It is natural to suggest that grounding LFI in the shallow regions is primarily controlled by the grounding mechanism, while the tensile strength parameter k_T is responsible for LFI in the deep regions of the Arctic

Ocean. This allows us to conduct separate optimization of $k_2$and k_T and significantly decrease the dimensions N^R of the optimization problem and computational costs. The chosen (~3-8) dimensions N^R of the control vectors allowed relatively fast (10-20 iterations) convergence of the CG minimization procedure and reasonable spatial variability of the LFI parameters.

Lemieux et al. (2015, 2016) and Itkin et al. (2015) developed LFI parameterizations for their coupled ice-ocean modeling systems configured for the entire Arctic. The parametrizations include two different algorithms. The first algorithm is based on a grounding scheme in which LFI can occur within a user-specified depth water depth limit, h_w. In multiple numerical experiments, Lemieux et al. (2015, 2016) estimated h_w=25m, while Wang et al., 2014 adopted the higher value of h_w=35m. Taking into account the estimates of the maximum sea ice sails (keels) of H_{sail}=4.88m (H_{keels}=45m) (Duncan et al, 2018), we utilized the estimate of h_w=35m proposed by Wang et al., 2014. This parameterization incorporates a maximum depth for the basal stress term in the momentum equation (see Eq. 1) in which LFI can form when the ice thickness exceeds a critical value, h_c discussed below. This approach simulates the process of the LFI formation due to "anchoring" in shallow regions of the Arctic shelves.

For the CG algorithm (Equations 10 - 14) we adopted the Fortran code from the Florida State University library[6], which is based on the algorithm proposed by Gilbert and Nocedal, (1992). In order to implement the CG algorithm together with the CICE6 model, it was re-written into several separate Fortran routines, which exchanged information between each other and multiple runs of the CICE6 model via the separate bash scripts. Matlab code was developed for the calculation of the cost function and cost function gradients from the output of the multiple CICE6 model runs. The developed combination of the bash scripts, Fortran and Matlab codes were validated with several test functions on a Linux server. Afterwards, these scripts were ported to the Navy High Performance Computers using the Cylc[7] scripting language (Gorman et al, 2018). The Cylc scripts managed all the runs on the HPC by providing the first guess fields, setting up the number of simulations for a given region and the number of control points (typically 8) and running until the convergence criteria was reached. Convergence was normally reached in 25 iterations or less.

8. Tensile Strength (k_T) Optimization

Based on the modified ice rheology including uniaxial tensile strength formulation, k_T (proposed by König, Beatty and Holland, 2010), LFI can form between chains of islands or in the straits as a result of ice "arches" (e.g. Kara Sea, Canadian Archipelago). König Beatty and Holland (2010) performed a series of experiments in which they varied the value of the ratio of the major and minor axes of the elliptical yield curve, *e*, and tensile strength, k_T. In these parameterizations, the values for the ice grounding scheme and isotropic tensile strength were not region dependent and did not vary spatially. Lemieux (2015, 2016) performed studies (at resolutions of 20-28 km) and found that the new parametrizations allow more accurate simulation of the LFI, but still the area and length of LFI in some regions is underestimated, particularly for the Laptev and Kara Seas, suggesting the necessity to incorporate non-uniform spatial variability into the LFI parametrization, or a more advanced algorithm of the LFI parametrization (e.g. Dupont et al., 2022).

We performed a series of tensile strength (k_T) optimization experiments for the Canadian Archipelago (Figure 8). Due to its large size, we divided the region into 4 smaller sub-regions (CA1-1 – CA1-4). The Cylc scripts were modified to optimize for k_T instead of k_1. The default $k_T = 0.2$ was specified as a first guess. However, when applying the minimization procedure to the entire CA1 region we found that some of the control k_T variables became negative and were not physically reasonable. We attributed this to the fact that arching LFI is a more complicated phenomenon than grounding LFI and depends on a proper combination of dynamical and geographical factors. For example, in the Nares Strait, arching LFI may not form every year (Ryan and Munchow, 2016). Thus, the absence of the arching LFI may require k_T to be

[6] https://people.sc.fsu.edu/~jburkardt/f77_src/cg_plus
[7] https://cylc.github.io/cylc-doc/7.9.3/singlehtml/index.html#document-index

zero in some regions, and afterwards the next iteration CG algorithm may easily make k_T to be negative. Formally, this problem may be resolved through the inclusion of the additional exponential term $f_{exp}(x) \sim w \exp[-\eta(k_{T,min} + k_T)]$ into the cost function (7). This term exponentially increases when k_T became negative, but incorporation of this term requires multiple numerical experiments for tuning the empirical parameters $w,\ \eta, k_{T,min}$. Because of this, instead of using a CG optimized value for k_T, we decided to define four constant k_T values for the four subregions through the gradual increase of k_1 and evaluation of the cost function (7) for each CICE6 run. Results for 2015-2016 and 2017-2018 are shown in Figure 11. Interestingly, the cost function for the CA1-4 regions in 2015-2016 clearly shows the presence of two minimums. One for the $k_T = 1.8$, and another for negative k_T. Similarly, in CICE6 runs for 2017-2018, the cost functions for the regions CA1-3 and CA1-4 have an almost flat area between 0 and 0.2. This explains the negative k_T values which were obtained in application of the CG gradient described above. Note also, that the optimal k_T values significantly increase the default value k_T=0.2 proposed by Lemieux et al. (2016). That can be explained by insufficient convergence of the EVP solver in the high resolution CICE6 simulations. As a result, artificial elastic oscillations in the velocity field increases LFI velocity criteria $|U_{LFI}| \leq 0.0005$ m/s and sea ice is not treated as LFI. Indeed, this ice practically does not move and may be treated as LFI as well, if we apply a weaker LFI criteria (e.g. $abs(\boldsymbol{u}) < |U_{LFI}| = 0.005$ m/s.) Given the unphysical results of k_T found in this optimization, we opted to set k_T to the physically reasonable value of 0.2 for all regions.

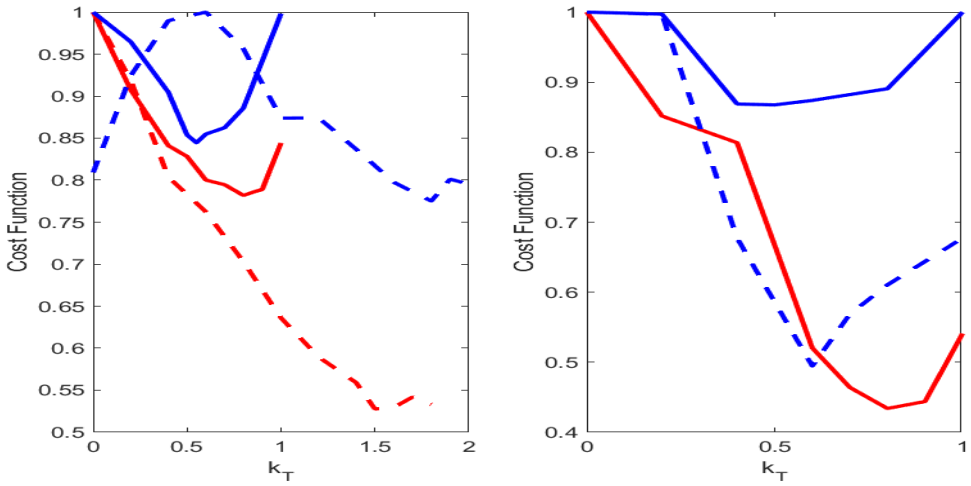

Fig. 11 Left panel: Cost functions evaluated for the CICE6 2015-2016 model runs for different sub-regions (CA1-1: red; CA1-2: red-dashed; CA1-3: blue; CA1-4: blue-dashed). Right panel: the same as on the left panel, but for 2017-2018 model runs.

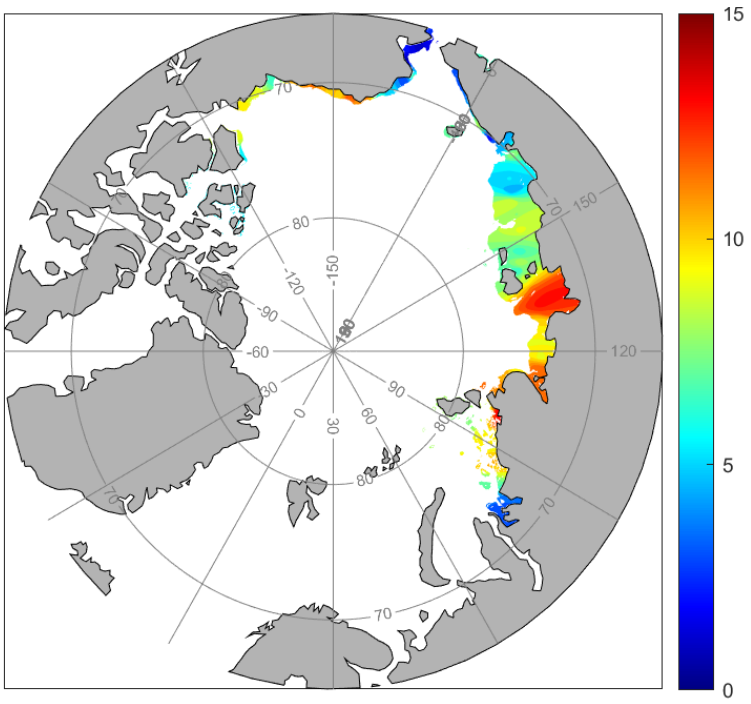

Fig. 12 *Map depicting optimized values for k_1 based on optimization experiments performed during the periods of Oct 1, 2015 – July 31, 2016 and Oct 1, 2017 – July 31, 2018. Note highest values in the East Siberian Sea.*

9. Results

After the optimized spatially varying parameters for k_1 (Fig. 12) were developed, we tested the results by performing simulations for all regions shown in Fig. 8. Note that Lemieux et al. (2015) used a constant value of k_1= 8.

We used constant default values of $k_2 = 15$ N m^{-3}, and $k_T = 0.2$. The same atmospheric forcing, initial conditions and boundary conditions that were used in the k_1 optimization experiments were used here. We performed a series of 3 experiments: 1) default run with LFI turned "off", 2) LFI turned "on" using optimized spatially values for k_1, and 3) run using default values suggested by Lemieux et al. (2015, 2016) with k_1 = 8, k_2 = 15 N m^{-3}, and k_T = 0.2 (no spatial variation for all parameters).

Figures 13 – 16 depict time series plots of LFI extent for these experiments for the period of Oct 1, 2017 – July 31, 2018. Note all the y-axis labels have the same range. In these plots, the red lines denote the simulation with LFI turned "off", the black line represents the optimized solution, the blue line represents the USNIC observed LFI extent, and the black dashed line denotes the simulation performed using the parameters recommended by Lemieux et al. (2015) without any spatial variation.

Figure 13 depicts an analysis of the results for ESS1 and ESS2 for the period of October 1, 2017 – July 31, 2018. In ESS1, an under-prediction of the LFI extent with the optimized solution is evident for the months of June and July. The landfast "off" simulation shows very little LFI. Using the "JFL" defaults we observe too much LFI versus the USNIC analysis. In the ESS2 region, we see more LFI with an over-prediction through April 2018 for the optimized solution, and a slight under-prediction in the summer period. Note how all the simulations show there is no more LFI by the end of July. For the month of June, the "JFL" results fall between the optimized and USNIC analysis. The ESS2 regions showed the maximum LFI extent for all regions analyzed in this study. The optimized solution versus JFL simulations showed very similar results, suggesting the optimized values for k_1 were close to the default value of 8.0.

Figure 14 illustrates the LFI extents for ESS3 and ESS4. We see very good agreement between the optimized solution and the USNIC analysis in ESS3, while the JFL simulation under-predicts the extent. ESS4 shows similar results between the optimized solution and the JFL simulation, where JFL is marginally closer to the USNIC observed extent. Overall, very good agreement is shown versus the USNIC analysis.

Figures 15 depicts the LFI extent for the three regions identified for the Chukchi Sea. Note the LFI extent is much smaller than for the East Siberia Sea. CS1 shows similar results for both experiments versus the USNIC analysis. CS2 shows an over-prediction from March – May 2018 for the JFL solution, and a large under-prediction for the optimized run. The probability map (Fig. 5) for the CS2 region shows that the presence of the LFI does not have a very high probability. Note, we analyzed the entire set of the LFI data and defined the area of grounded LFI as an area with the probability > 10% and depths < 35m. These procedures removed some areas where LFI could be formed. Mathematically that is reasonable, because we have some errors in the LFI data. Physically, taking into account the estimates of the maximum sea ice sails (keels) of H_{sail} =4.88m (H_{keels} =45m) (Duncan et al, 2018), we utilized the estimate of h_w=35m proposed by Wang et al., 2014 it is reasonable to use a depth of 35m as a limit. But these conditions (limitations) do not allow for the development of LFI in some areas. In the case of JFL's k_1, formally LFI can be developed even at a 100m depth, because JFL compares sea ice thickness H with local depth h/k_1. So, for example, if CICE6 for some reason has the ice thickness of 100m/8=12.5m, the grounded LFI will be formed in 100m depth even though that is not a realistic scenario. In our case we made a barrier of 35m for the formation + 10% limitation. Figure 15c shows a slight under-prediction for the optimized solution and a significant over-prediction using the JFL default criteria. The optimized solution for CS3 is superior to the JFL solution.

Figure 16a shows a time-series of the LFI extent for the Beaufort Sea (BE7). We see a reasonable comparison between the optimized solution, USNIC analysis and JFL simulation. Overall, the optimized solution shows an under-prediction beginning in April 2018. The JFL solution shows a closer agreement to the USNIC analysis. Figure 16b shows a comparison between the 3 model simulations and the USNIC analysis for the Laptev Sea. The JFL results show a clear over-prediction. The optimized solution also shows an over-prediction through March 2018, and a slight under-prediction beginning in April 2018.

Regarding the under-prediction for CS2 and BE7, future efforts to consider include: a) removing the 10% limitation, b) removing the 35m restriction for some regions (e.g. CS2), and c) slightly increase k_1. Both "a" and "b" will result in the increase of the "k_1 stencil". "c" is the "ad hoc" suggestion of course, but it may help.

Our optimization technique works well in the regions with one form of the LFI (where k_1 is dominant), i.e. in the Siberian Sea. For the regions with 2 forms of the LFI (where grounding and tensile strength are important), we are either missing LFI in the deep areas or have to specify non-physically high k_T, or extend grounding for the depths > 35m. Both are non-physical, and thus the problem with LFI in the deep regions need additional theoretical attention.

Figure 17 depicts the LFI extent on May 3, 2018 in the Beaufort and Chukchi Sea. The blue line denotes the optimized solution while the green line shows the USNIC analyzed extent. The red line shows the results with LFI turned "off". The inset shows a zoomed in region in the Beaufort Sea. For this particular period, the optimized solution shows the LFI extent south of the observed extent. Figure 18 shows the LFI extent for the East Siberian and Laptev Sea. The East Siberian region (comprised of 4 sub-regions) shows good agreement between the optimized solution and the USNIC analysis.

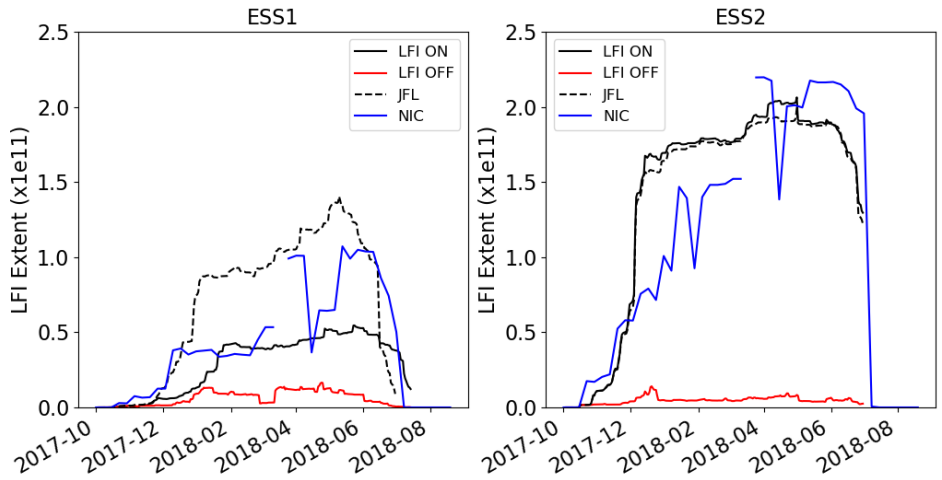

Fig. 13 *Landfast ice extent (m^2) for the East Siberian Sea Region 1 (left) and 2 (right) for the period of October 1, 2017 – August 1, 2018. Black line represents optimized solution with LFI activated, red line denotes LFI extent with landfast set to "off", black dashed line represents LFI using defaults from Lemieux et al. (2016) with no spatial variability. Blue line represents USNIC's observed LFI extent.*

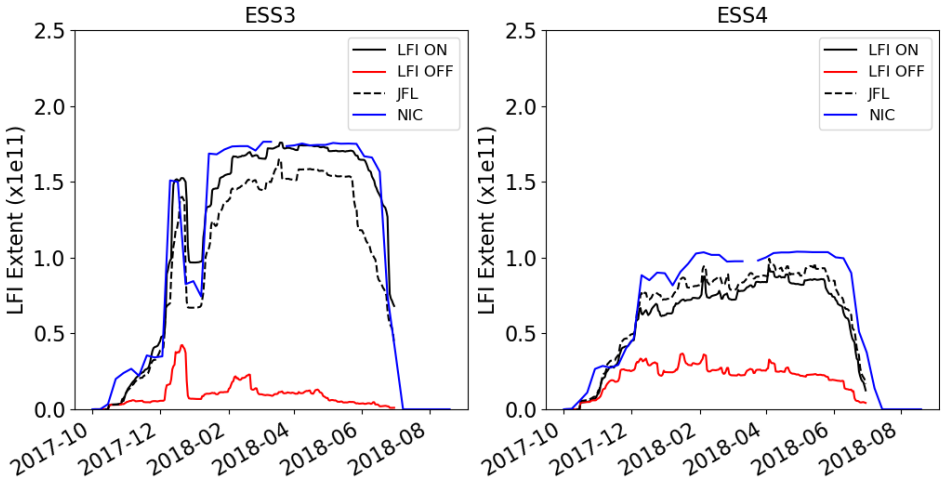

Fig. 14. *Same as Fig. 13, except for East Siberian Sea 3 (left) and East Siberian Sea 4 (right).*

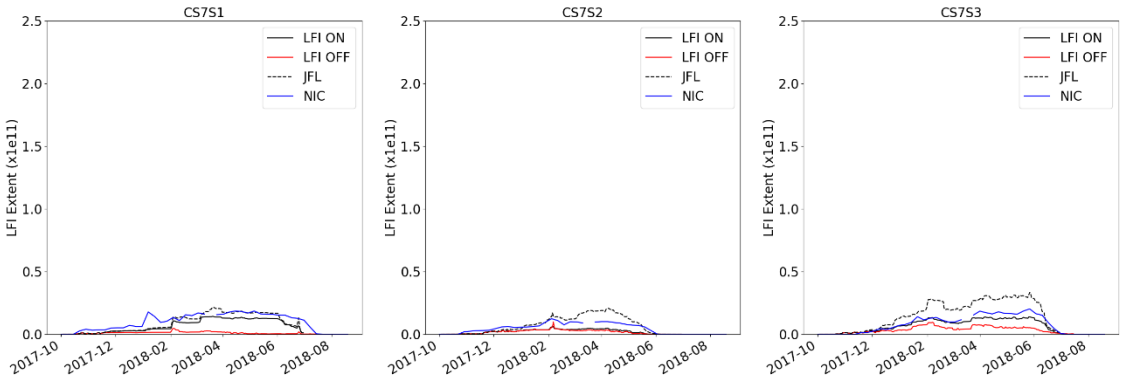

Fig. 15 *Same as Fig 13, except for Chukchi Sea 1 (left), Chukchi Sea 2 (middle), and Chukchi Sea 3 (right).*

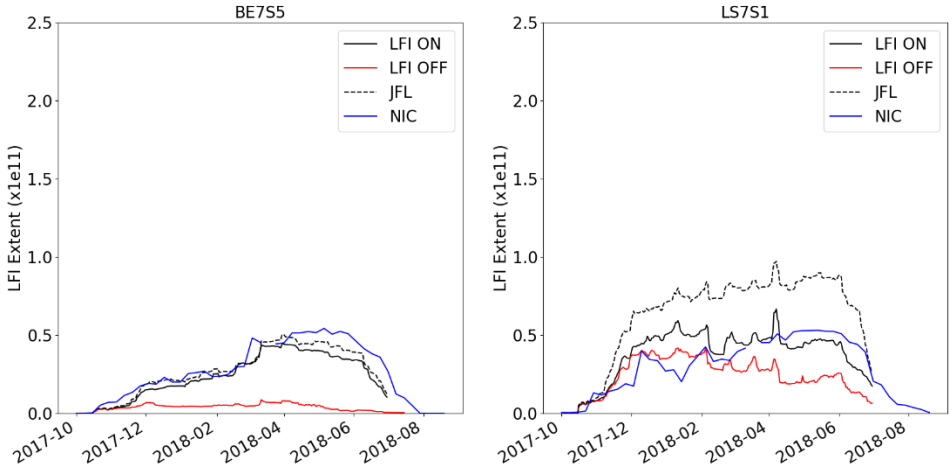

Fig. 16 *Same as Fig. 13, except for Beaufort Sea (left) and Laptev Sea (right).*

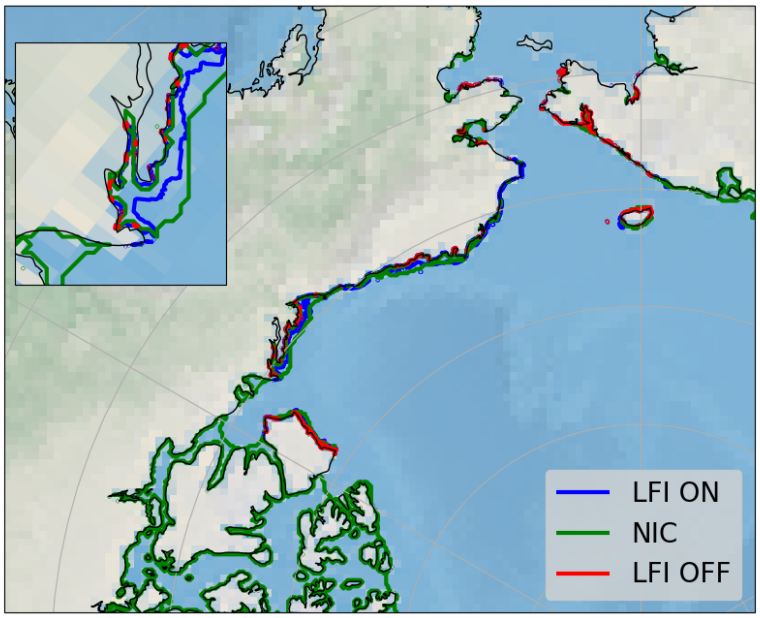

Fig. 17 LFI extent on May 3, 2018 for Beaufort and Chukchi Seas superimposed on sea ice concentration (%). White line denotes USNIC observed ice edge. Green line represents optimized solution. Red line is from model simulation with LFI turned off. Inset shows detail for Beaufort Sea.

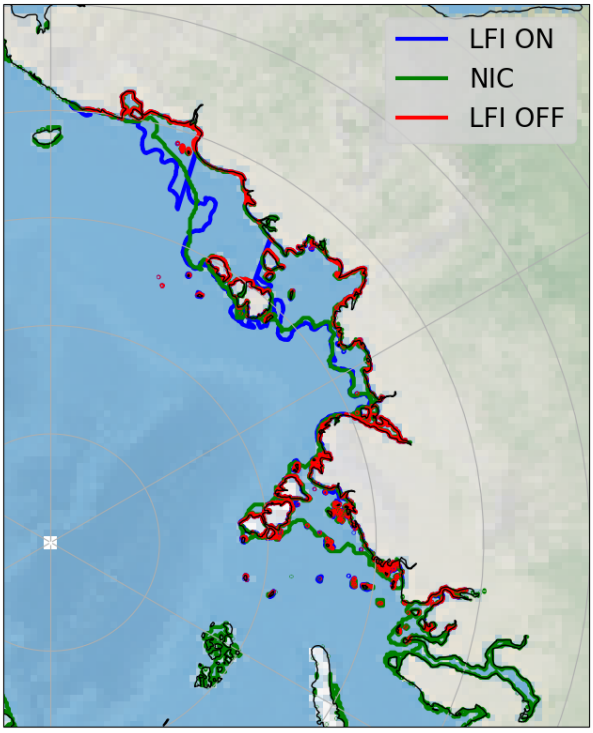

Fig. 18 *Same as Fig. 17 but for East Siberian and Laptev Sea*

10. Summary and Conclusions

In this report we document the technique used to develop spatially varying LFI grounding parameter, k_l, in the CICE6 model. Previously Navy sea ice models have not included LFI, which can account for approximately 10% of the ice in the Arctic. This is important for several reasons: 1) the placement of the LFI boundary separates ice that does not move from the "pack ice" which is always moving and is under the influence of surface wind forcing and to a lesser extent the ocean currents below the ice. 2) This is critical as it can affect the formation of polynyas or "flaw leads" which are evident in satellite imagery as regions of lower ice concentration and important for air-sea heat exchange.

We divided the Arctic into 10 sub-regions covering the Beaufort, Chukchi, East Siberian and Laptev Seas. Using a conjugate gradient optimization technique, we developed spatially varying LFI parameters based on a series of experiments performed for the periods of Oct 1, 2015 - July 31, 2016 and Oct 1, 2017 - July 31, 2018. We found the best results for the East Siberian Sea in comparison with USNIC data. In this region, grounding is the dominant factor in the formation of LFI. In regions such as the Laptev Sea where both grounding and ice arching can contribute to LFI formation, our technique under-predicts the formation of LFI. This may be attributed to our limitation of a maximum water depth of 35 m for grounding and our decision to avoid non-physical high values for k_T which could have resulted in more LFI.

Future work should include performing optimization experiments for the Kara Sea, a region not included in this study. We would like to extend our optimization for additional years to provide a more realistic representation of the LFI characteristics in the Arctic. We also need to revisit our criteria in determining where LFI can form based on historical data. Our choices in this project may have limited the formation in some regions. The spatially varying grounding parameter k_l developed in this study will be incorporated into a pan-Arctic 1/25° grid for further testing. This will eliminate any possible contamination introduced by boundary conditions utilized in our 10 regional domains used in this study.

The spatially-varying k_l coefficients developed under this 6.2 project are being incorporated into the ESPC v3 deterministic modeling system. We are also developing a LFI database to be used as part of the Coupled Ocean Atmosphere Mesoscale Prediction System (COAMPS). The k_l coefficients will be interpolated "on-the-fly" for any CICE6 regional Arctic grid, typically at a 1km resolution.

11. Acknowledgements

The authors thank Mr. James Dykes (formerly of NRL) for designing the Cylc scripts used in this study. The scripts were ported to the Navy DSRC SGI platforms, where Mr. Dykes performed numerous testing and created useful documentation of the entire process. We also that Dr. Nikolai Nezlin (NOAA), who helped us with initial processing of the geo-maps from the NSIDC archive.

12. References

Antonova, S. (2011): Spatial and temporal variability of the fast ice in the Russian Arctic-MS Thesis, Univ. of Hamburg, Germany, 37 pp.

Divine, D. V., R. Korsnes, and A. P. Makshtas, (2004): Temporal and spatial variation of shore-fast ice in the Kara Sea. *Cont. Shelf Res.*, 24, 1717-1736.

Duncan, K., Farrell, S., Connor, L., Richter-Menge, J., Hutchings, J., & Dominguez, R. (2018): High-resolution airborne observations of sea-ice pressure ridge sail height. Annals of Glaciology, 59(76pt2), 137-147. doi:10.1017/aog.2018.2

Dupont F, D. Dumont, J-F Lemieux, E. Dumas-Lefebvre, and A. Caya (2022): A probabilistic seabed–ice keel interaction model The Cryosphere, 16, 1963–1977, https://doi.org/10.5194/tc-16-1963-2022.

Egbert, G.D., and S.Y. Erofeeva, (2002): Efficient inverse modeling of barotropic ocean tides, J. Atmos. Oceanic Technol., 19(2), 183-204.

Gilbert, J. C. and J. Nocedal, (1992): Global Convergence Properties of Conjugate Gradient Methods, SIAM Journal on Optimization, Volume 2, pages 21-42.

Gorman, R. M. and Oliver, H. J (2018): Automated model optimisation using the Cylc workflow engine (Cyclops v1.0), Geosci. Model Dev., 11, 2153–2173, https://doi.org/10.5194/gmd-11-2153-2018.

Granskog M.A., Vihma T., Pirazzini R. & Cheng B. (2006): Superimposed ice formation and surface energy fluxes on sea ice during the spring melt/freeze period in the Baltic Sea. Journal of Glaciology 52, 119-127.

Hunke, E. C. (2001): Viscous-plastic sea ice dynamics with the EVP model: Linearization issues, J. Comput. Phys., 170, 18– 38.

Hunke, E. C., Lipscomb WH. (2008): CICE: The Los Alamos sea ice model. Documentation and software user's manual version 4.0. Technical Report LA-CC-06-012, Los Alamos National Laboratory.

Ilich, N. (2014):An effective three-step algorithm for multi-site generation of weekly stochastic hydrologic time series. Hydrol. Sci. J., 59(1), 85–98.

Itkin, P., M. Losch and R. Gerdes (2015): Landfast ice affects the stability of the Arctic halocline: Evidence from a numerical model, J. Geophys. Res. Oceans, 120, 2622-2635, doi:10.1002/2014JC010353.

Jacobs, J. D., R. G. Barry, and R. L. Weaver (1975): Fast ice characteristics, with special reference to the eastern Canadian Arctic. Polar Rec., 110, 521-536.

Khachaturyan, A., Semenovskaya, S., Vainshtein B., Armen (1979): Statistical-Thermodynamic Approach to Determination of Structure Amplitude Phases. Soviet Physics, Crystallography. **24** (5): 519–524.

König Beatty, C. and D. M. Holland (2010): Modeling Landfast Sea Ice by Adding Tensile Strength. *J. Phys. Oceanogr.*, 40, 185-198.

Lemieux, J.-F., L. B.Tremblay, F. Dupont, M. Plante, G. C. Smith and D. Dumont (2015): A basal stress parameterization for modeling landfast ice, J. Geophys. Res. Oceans, 120, doi:10.1002/2014JC010678.

Lemieux, J.-F., F. Dupont, P. Blain, F. Roy, G. C. Smith, and G. M. Flato (2016): Improving the simulation of landfast ice by combining tensile strength and a parameterization for grounded ridges, J. Geophys. Res. Oceans, 121, doi:10.1002/2016JC012006.

Lewis, A.S. and Overton, M.L. (2013): Math. Program, 141: 135. doi:10.1007/s10107-012-0514-2

Lipscomb, W. H., E. C. Hunke, W. Maslowski, and J. Jakacki (2007): Ridging, strength, and stability in high-resolution sea ice models, J. Geophys. Res., 112, C03S91, doi:10.1029/2005JC003355.

Mahoney, A., H. Eicken, A. G. Gaylord, and L. Shapiro (2007): Alaska landfast sea ice: Links with bathymetry and atmospheric circulation, J. Geophys. Res., 112, C02001, doi:10.1029/2006JC003559.

Mahoney A.R., Eicken H., Gaylord A.G., and Gens R. (2014):Landfast sea ice extent in the Chukchi and Beaufort Seas: The annual cycle and decadal variability. Cold Regions Science and Technology, **103**: 41–56.

Mahoney, A (2018): Landfast Sea Ice in a Changing Arctic (in Arctic Report Card 2018], https://arctic.noaa.gov/Report-Card/Report-Card-2018/ArtMID/7878/ArticleID/788/Landfast-Sea-Ice-in-a-Changing-Arctic

Nikishin, A.M., Startseva, K.F., Verzhbitsky, V.E. et al. (2019): Sedimentary Basins of the East Siberian Sea and the Chukchi Sea and the Adjacent Area of the Amerasia Basin: Seismic Stratigraphy and Stages of Geological History. Geotecton. 53,635–657. https://doi.org/10.1134/S0016852119060104.

Panteleev, G., Yaremchuk, M., Stroh, J. N., Francis, O. P., and Allard, R. (2020): Parameter optimization in sea ice models with elastic–viscoplastic rheology, The Cryosphere, 14, 4427–4451, https://doi.org/10.5194/tc-14-4427-2020.

Pincus, M. *(1970):* A Monte-Carlo Method for the Approximate Solution of Certain Types of Constrained Optimization Problems". Journal of the Operations Research Society of America. **18** (6): 967–1235. doi:10.1287/opre.18.6.1225.

Rothrock, D. A. (1975): The energetics of the plastic deformation of pack ice by ridging, J. Geophys. Res., 80, 4514– 4519.

Ryan, P. A. and A. Münchow (2017): Sea ice draft observations in Nares Strait from 2003 to 2012, *J. Geophys. Res. Oceans*, 122, 3057–3080, doi:10.1002/2016JC011966.

Selyuzhenok, V., T. Krumpen,A. Mahoney, M. Janout, and R. Gerdes (2015): Seasonal and interannual variability of fast ice extent in the southeastern Laptev Sea between1999 and 2013,J. Geophys. Res. Oceans, 120, 7791–7806, doi:10.1002/2015JC011135

SIGRID-3: A vector archive format for sea ice charts. JCOMM Technical Report No. 23, 2010. https://library.wmo.int/doc_num.php?explnum_id=9270.

Wang, J., K. Mizobata, X. Bai, H. Hu, M. Jin, Y. Yu, M. Ikeda, W. Johnson, W. Perie, and A. Fujisaki (2014): A modeling study of coastal circulation and landfast ice in the nearshore Beaufort and Chukchi seas using CIOM, J. Geophys. Res. Oceans, 119, 32853312, doi:10.1002/2013JC009258